

Ferroelectric HfO₂ and the importance of strain

Sesha Sai Behara  and Anton Van der Ven*

Materials Department, University of California, Santa Barbara, Santa Barbara, California 93106, USA



(Received 7 February 2022; revised 4 April 2022; accepted 20 April 2022; published 5 May 2022)

Ferroelectric oxides based on HfO₂ show tremendous promise for the next generation of memory and logic devices. The ferroelectric polymorph is one of several that can be derived from the high symmetry cubic fluorite structure of HfO₂. A single grain of HfO₂ may consist of a coherent mixture of multiple orientational and translational variants of different polymorphs. Here, we use symmetry-adapted strain-order parameters to elucidate the relationship between the different HfO₂ polymorphs and their symmetrically equivalent variants. We use first-principles electronic structure methods to identify minimum energy pathways and map them in subspaces of the symmetry-adapted strain order parameters. We next investigate the atomic structure of domain boundaries that separate coexisting variants of ferroelectric HfO₂. We rely on Gibbsian excess quantities and a precise specification of mechanical boundary conditions to describe the thermodynamic properties of domain boundaries. Our first-principles calculations show that the O and Hf shuffle arrangement within a domain boundary is closely related to the intermediate shuffle patterns of the homogeneous pathways between ferroelectric variants. Furthermore, the preferred structure within a boundary is very sensitive to local strain constraints imposed by the adjacent ferroelectric variants, leading to highly anisotropic domain boundary energies.

DOI: [10.1103/PhysRevMaterials.6.054403](https://doi.org/10.1103/PhysRevMaterials.6.054403)

I. INTRODUCTION

Ferroelectric materials are of interest for high-density electronics such as ferroelectric field-effect transistors (FeFET) [1–4] and ferroelectric random-access memory (FRAM) [5,6]. The ever-increasing desire to reduce device dimensions, however, is leading to significant materials challenges [7,8]. Traditional perovskite ferroelectrics, for example, lose their ferroelectric properties below a thickness of 1.2 nm [9–11] and their small band gaps make them susceptible to high leakage currents [12,13]. They often also contain numerous chemical elements [1,14–19], making them difficult to deposit, especially in 3-dimensional geometries [20,21]. Furthermore, many promising perovskite ferroelectrics contain Pb [1,15,22–24], a large and volatile element that is not only difficult to incorporate during atomic layer deposition (ALD) [21,25], but is also toxic.

The report of a ferroelectric form of HfO₂ in 2011 [26,27] has made this material a prime candidate for multiple logic and memory devices [28,29]. The ferroelectric form of HfO₂ is identified to be a noncentrosymmetric orthorhombic structure belonging to the Pca2₁ space group [26,27,30]. Ferroelectric HfO₂ exhibits the remarkable property that its ferroelectric character becomes stronger as its dimensions get smaller [31]. A recent report demonstrated ferroelectric behavior in a 1-nm-thick HfO₂ based film [32]. Electric dipoles in HfO₂ are extremely localized (~ 0.3 nm) and stable due to flat phonon bands [33]. This enables ferroelectric switching at an angstrom scale, which is not possible in conventional perovskites [33]. For applications that need thicker layers or

to minimize leakage currents, it is possible to incorporate ferroelectric HfO₂ in superlattice structures or to combine it with thin layers of other oxides, such as Al₂O₃, without negatively affecting ferroelectric properties [28,34,35]. HfO₂ based oxides are also compatible with current CMOS chemistry and manufacturing, and have already been in widespread use in Si-based electronics as high-k dielectrics [28,29]. The processing technology of HfO₂ based heterostructures with ALD is mature and the chemistry is easy to integrate in 3-dimensional architectures [28,29]. Ferroelectric HfO₂ is not only very promising for FRAM and FeFET, but also for ferroelectric tunnel junctions (FTJ), synapses for neuromorphic computing and devices that exploit negative capacitance [28,29,36,37].

HfO₂ has many polymorphs depending on its temperature, state of stress or strain, and thermomechanical history [38–41]. Most of these polymorphs can be derived from a common cubic fluorite structure through the application of small symmetry breaking distortions. The structural commonality among the HfO₂ polymorphs allows for the coherent coexistence of several polymorphs within a single grain [42,43]. It also allows for the coherent coexistence of symmetrically equivalent orientational and translational variants of the same polymorph. The coherent coexistence of multiple variants of the ferroelectric polymorph of HfO₂, for example, enables the switching of the net polarization of a grain through the enlargement of favorably oriented domains at the expense of less favorably oriented domains [44–48]. This occurs through the migration of domain walls, the boundaries that separate different variants of a polymorph that coexist coherently within the same grain [49–51].

In this paper, we build on and unify previous first-principles studies of HfO₂ [38,49–59] and clarify the re-

*avdv@ucsb.edu

relationship between the different polymorphs of HfO_2 with the help of symmetry-adapted strain-order parameters. We systematically identify pathways that connect different HfO_2 polymorphs and their symmetrically equivalent variants and map them in subspaces of symmetry-adapted strain-order parameters. Several of the pathways identified in this study have lower energies than those identified in previous studies. We also explore the energies and atomic structures of domain boundaries, using a Gibbsian approach that relies on excess quantities to describe the thermodynamic properties of domain boundaries. The atomic structure within the studied domain boundaries are found to be very similar to the intermediate states of the homogeneous pathways that connect different variants. We find that the imposed strains and stresses play an important role in determining the energy and atomic structure of domain boundaries. This leads to highly anisotropic domain boundary energies.

II. METHODS

All electronic structure calculations were performed using the Vienna *ab initio* simulation package (VASP) [60–62] with the projector-augmented wave (PAW) method [63,64]. The SCAN exchange-correlational functional [65] was used as it is capable of accurately predicting the structure and relative stabilities of oxides [66]. The total energy was converged to 10^{-5} eV and the forces on atoms were converged to 0.02 eV/Å when performing atomic relaxations. An automatic k -point mesh generation scheme was used with the length parameter R_k set equal to 32 Å. A plane wave energy cut-off of 520 eV was used for all the calculations. Spontaneous polarization calculations were performed using Berry phase expressions [67] as implemented within the VASP package. To overcome the *multivaluedness* of polarization in periodic cells, dipole moments of different variants of HfO_2 were determined relative to a close nonpolar structure [68]. Solid-state nudged elastic band (*ss*-NEB) calculations were performed using the transition state tools for VASP [69–71]. A climbing image method [72] with a Quick-Min optimizer [73] was used to find the saddle points along the minimum energy path. The forces on atoms are converged to 0.03 eV/Å. A crystal mapping algorithm was used [74] to determine symmetry relations between various phases and variants of HfO_2 .

III. RESULTS

A. Crystallography and strain order parameters

The high temperature phase of HfO_2 , referred to as c- HfO_2 , has a cubic fluorite structure with space group $\text{Fm}\bar{3}\text{m}$. The Hf atoms of c- HfO_2 reside on an fcc sublattice with the oxygen atoms filling the interstitial tetrahedral sites of the Hf sublattice. A variety of lower-symmetry polymorphs, including the tetragonal (t- HfO_2 , space group $\text{P}4_2/\text{nmc}$), orthorhombic (o- HfO_2 , space group $\text{Pca}2_1$) and monoclinic (m- HfO_2 , space group $\text{P}2_1/\text{c}$) polymorphs, can be generated upon straining the c- HfO_2 unit cell and displacing the atoms within the nonprimitive cubic unit cell of c- HfO_2 . The degree and nature of these distortions become clear with the use of symmetry-adapted strain and shuffle order parameters. To track the strains that relate one polymorph to another, we use the following strain

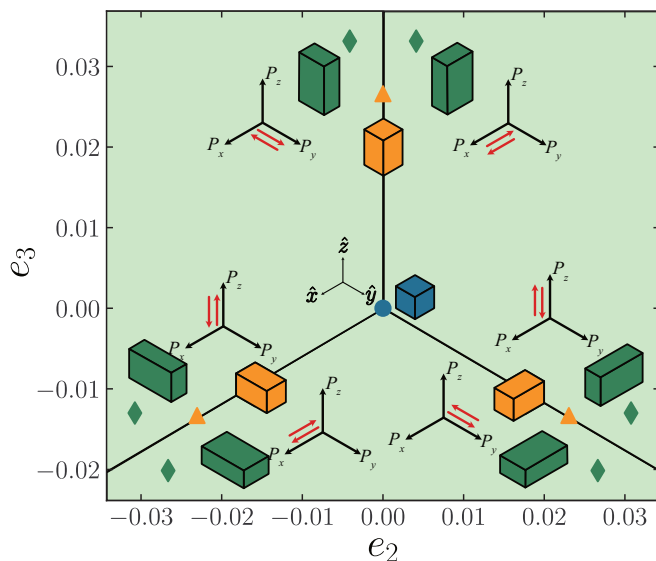


FIG. 1. The placement of the c- HfO_2 (blue circle), t- HfO_2 (orange triangles), and o- HfO_2 (green diamonds) polymorphs in $e_2 - e_3$ space. The cubic phase c- HfO_2 serves as the reference crystal to measure strain and appears at the origin. Also shown are the electric polarization vectors for each orientational variant of o- HfO_2 . The distortions of the unit cells are exaggerated to highlight the nature of the distortion.

order parameters [75]:

$$\begin{pmatrix} e_1 \\ e_2 \\ e_3 \\ e_4 \\ e_5 \\ e_6 \end{pmatrix} = \begin{pmatrix} \frac{(E_{xx} + E_{yy} + E_{zz})}{\sqrt{3}} \\ \frac{(E_{xx} - E_{yy})}{\sqrt{2}} \\ \frac{(2E_{zz} - E_{xx} - E_{yy})}{\sqrt{6}} \\ \sqrt{2}E_{yz} \\ \sqrt{2}E_{xz} \\ \sqrt{2}E_{xy} \end{pmatrix}, \quad (1)$$

where the E_{xx} etc. refer to Cartesian strains applied to a cubic reference crystal of HfO_2 with its cubic axes aligned with the Cartesian axes. The first symmetry-adapted order parameter e_1 measures symmetry preserving volumetric changes when strains are infinitesimal or when using the Henky strain metric [75]. The next two strain order parameters, e_2 and e_3 , measure tetragonal and orthorhombic distortions of the cubic unit cell. The last three strain order parameters, e_4 , e_5 , and e_6 , are shear strains. Figure 1 shows the placement of different polymorphs in the subspace spanned by e_2 and e_3 , with c- HfO_2 residing at the origin.

The tetragonal t- HfO_2 polymorph can be obtained from c- HfO_2 through a combination of an oxygen shuffle and a tetragonal lattice strain. There are three symmetrically equivalent tetragonal strains that can be applied to the cubic reference crystal. One t- HfO_2 variant emerges upon the application of a tetragonal elongation along the \hat{z} axis of the cubic phase coupled with a uniform contraction along the \hat{x} and \hat{y} axes. This deformation corresponds to a finite value of e_3 at $e_2 = 0$ and is illustrated in Fig. 1 as the orange triangle on the positive e_3 axis. Symmetrically equivalent tetragonal strains can also be applied along the \hat{x} axis and along the \hat{y}

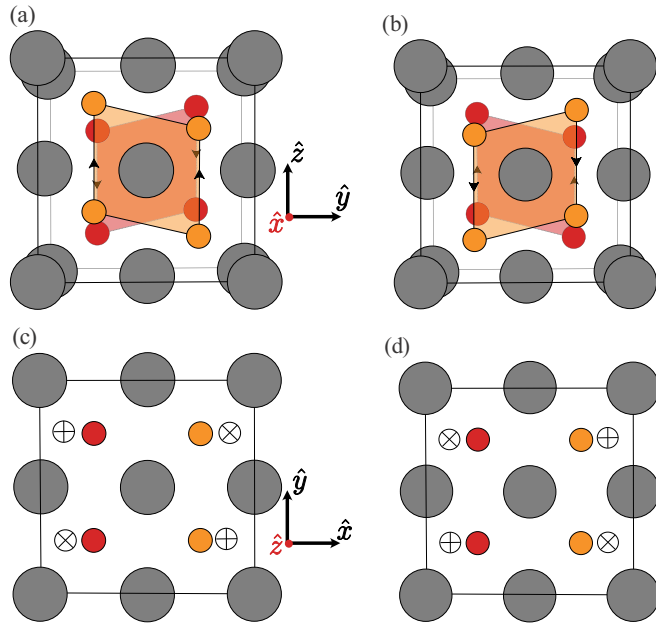


FIG. 2. Translational variants of tetragonal HfO₂ showing (a) the $+\hat{z}$ shuffle viewed down the \hat{x} axis, (b) the $-\hat{z}$ shuffle viewed down the \hat{x} axis, (c) the $+\hat{z}$ shuffle viewed down the \hat{z} axis and (d) the $-\hat{z}$ shuffle viewed down the \hat{z} axis. The red oxygens occupy the (400) plane whereas the orange oxygens occupy (400) plane translated by $[1/2\ 0\ 0]$.

axis, which appear in e_2 - e_3 space along lines that have been rotated by $\pm 120^\circ$ relative to the e_3 axis as shown in Fig. 1.

Each tetragonal variant undergoes an oxygen shuffle parallel to the tetragonal axis. For the tetragonal distortion along the \hat{z} axis, columns of oxygen parallel to the $\langle 001 \rangle$ direction shuffle up and down in a checkerboard pattern within the (001) plane. There are two translational variants of the \hat{z} shuffle. The shuffle distortion can be realized with a single phonon mode of c-HfO₂ (a X_2^- phonon mode), with a positive amplitude generating one translational variant and a negative amplitude generating the other translational variant [54]. We refer to these translational variants as $+\hat{z}$ and $-\hat{z}$, respectively as shown in Fig. 2. Since there are two translational variants for each of the three orientational tetragonal variants, a total of six tetragonal variants can form from a common high temperature c-HfO₂ crystal.

Each tetragonal variant can undergo orthorhombic strains, leading to two symmetrically equivalent orthorhombic distortions applied to a common tetragonal variant. The \hat{z} tetragonal variant along the e_3 axis, for example, can deform to orthorhombic symmetry through the activation of either a positive or a negative e_2 strain. Figure 1 shows two symmetrically equivalent orthorhombic distortions (green diamonds) of the \hat{z} oriented tetragonal variant. Rotating these strains by $\pm 120^\circ$ in e_2 - e_3 space yields the symmetrically equivalent orthorhombic distortions relative to the \hat{x} and \hat{y} tetragonal variants.

The ferroelectric orthorhombic form of HfO₂, (o-HfO₂) can be generated by applying additional atomic shuffles to the nearest tetragonal variant. As an illustration, consider the \hat{z} tetragonal variant along the e_3 axis in Fig. 1. An application

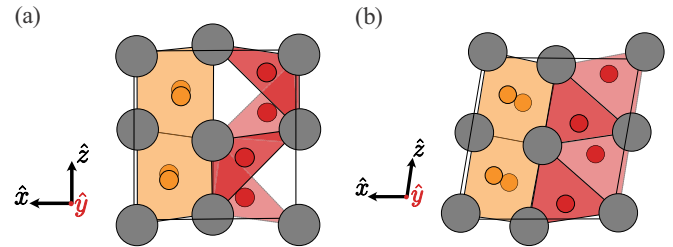


FIG. 3. The (a) orthorhombic and (b) monoclinic structures. Both structures have oxygen that are coordinated by four Hf (orange polyhedra) and three Hf (red polyhedra). The fourfold and threefold coordinated oxygen segregate to alternating planes that are parallel to the yz plane.

of a negative e_2 leads to an orthorhombic cell where the lattice vector parallel to \hat{x} is shortened relative to that parallel to \hat{y} . For this orientational variant of the orthorhombic cell, the a and b lattice vectors are parallel to the \hat{x} and \hat{y} directions, respectively, while the c lattice vector is parallel to the \hat{z} direction. In o-HfO₂, four of the eight oxygen ions per unit cell remain tetrahedrally coordinated by Zr (albeit off-centered), while the other four oxygen displace to triangular faces of the Zr tetrahedra, leading to threefold coordination [76]. The ordering of fourfold and threefold coordinated oxygen occurs in layers that are perpendicular to the short a axis of the orthorhombic cell. This is illustrated in Fig. 3(a). The layered ordering of fourfold and threefold coordinated oxygen ensures that each Hf is coordinated by seven oxygen ions.

There are six orientational variants of o-HfO₂ that can be derived from a common c-HfO₂ as illustrated by the green diamonds in Fig. 1. Each orientational variant can in turn host eight symmetrically equivalent oxygen shuffles, leading to a total of 48 symmetrically equivalent variants of o-HfO₂ having a common cubic reference crystal. The eight symmetrically equivalent oxygen shuffles for a particular orientational variant are shown in Fig. 4. The layers of fourfold and threefold coordinated oxygen are indicated by the orange and red atoms, respectively, and are perpendicular to the a lattice vector of the orthorhombic cell. These variants have been derived from a \hat{z} -shuffled tetragonal variant (the \hat{z} axis points out of the page in Fig. 4). For a particular orientational variant of the orthorhombic form, four oxygen shuffles are derived from a $+\hat{z}$ tetragonal shuffle (1, 4, 5, and 8 in Fig. 4) while the other four oxygen shuffles derive from a $-\hat{z}$ tetragonal shuffle (2, 3, 6, and 7 in Fig. 4). The o-HfO₂ lacks an inversion symmetry and therefore has an electric polarization. The polarization directions for each orientational variant are shown in Fig. 1. The polarization vector is parallel to the planes of fourfold and threefold coordinated oxygen but is perpendicular to the tetragonal axis of the tetragonal variant that it is derived from, thereby making it parallel to the b lattice vector of the orthorhombic cell. This is illustrated in Fig. 4 by the black arrow. The value of spontaneous polarization as calculated with SCAN is $45.75\ \mu\text{C}/\text{cm}^2$, which is in good agreement with the experimental value [77]. The oxygen shuffle within each orientational variant determines whether the polarization is positive or negative. The relation between the atomic shuffles

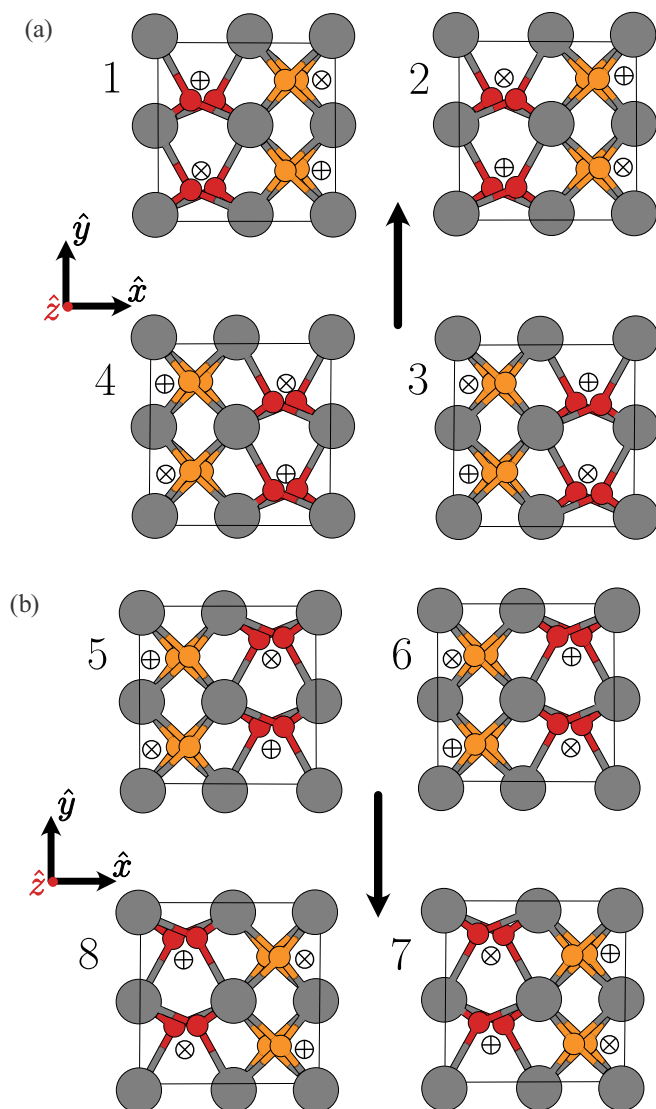


FIG. 4. All 8 symmetrically equivalent shuffle variants of an orientational variant of o-HfO₂. The 8 shuffle variants have been derived from a \hat{z} tetragonal variant that has undergone a negative e_2 strain. For this orientational variant of the orthorhombic unit cell, the a and b lattice vectors are parallel to the \hat{x} and \hat{y} axes, respectively, while the c lattice vector is parallel to the \hat{z} axis. (a) shows variants 1 to 4 and (b) shows variants 5 to 8, both in clockwise order. Variants 1, 4, 5, and 8 have a $+\hat{z}$ shuffle whereas variants 2, 3, 6, and 7 have a $-\hat{z}$ shuffle. Black arrows indicate the direction of the electric polarization. \oplus indicates that the oxygen shuffle is coming out of the plane whereas \otimes indicates the shuffle is going into the plane.

of o-HfO₂ and phonon modes of c-HfO₂ has been described in detail by Qi and Rabe [54].

The monoclinic form of HfO₂ (m-HfO₂) can be derived from t-HfO₂ in a manner that is similar to that described for o-HfO₂. A particular monoclinic variant can be obtained by first applying an orthorhombic strain to a tetragonal variant in e_2 - e_3 space followed by an application of a shear strain to produce a monoclinic unit cell [76]. This is illustrated in Fig. 5 for the four orientational variants of the monoclinic form that can be derived from a tetragonal \hat{z} variant. Application of a negative e_2 strain to a tetragonal \hat{z} variant, for example, generates an

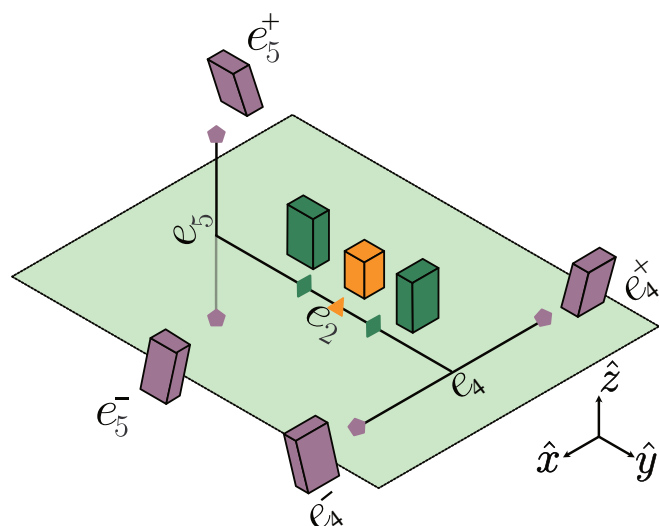


FIG. 5. A strain map in $e_2 - e_4 - e_5$ space at a finite value of e_3 showing the relationship between the tetragonal, orthorhombic and monoclinic polymorphs derived from a \hat{z} tetragonal variant [76]. Two monoclinic orientational variants can be derived from each orthorhombic variant. There are 4 shuffle variants for each monoclinic strain.

orthorhombic unit cell that can then be sheared by a positive or negative e_5 strain to generate two orientational variants of the monoclinic unit cell. Four orientational variants of the monoclinic unit cell can be obtained from each tetragonal distortion, leading to a total of twelve orientational variants of the monoclinic unit cell that can be derived from a common cubic reference.

The oxygen shuffles in m-HfO₂ have much in common with those in o-HfO₂. Similar to o-HfO₂, the oxygen of m-HfO₂ shuffle to form alternating layers of fourfold and threefold coordinated oxygen [76]. For the monoclinic variant obtained from a tetragonal \hat{z} shuffle upon application of a negative e_2 strain (Fig. 5) these layers are parallel to the (100) planes. Figure 3(b) shows the alternating layers of fourfold (orange polyhedra) and threefold (red polyhedra) coordinated oxygen. A crucial difference between the shuffle of m-HfO₂ and that of o-HfO₂ is the arrangement of oxygen in the threefold coordinated layers. This is illustrated in Fig. 6, which shows a projection of the threefold coordinated oxygen ions of the (100) layers of the monoclinic and orthorhombic forms. The particular ordering of the oxygen ions over threefold coordinated sites of o-HfO₂ is responsible for the electric polarization.

B. Pathways between different polymorphs

The stability of different polymorphs of HfO₂ depends on temperature and state of strain. In some instances, multiple polymorphs can coexist within the same grain, where one polymorph is the stable phase and the others are metastable phases [42]. In this context, it is of interest to explore minimum energy pathways connecting the different polymorphs of HfO₂. Similar to cubic ZrO₂ [78,79], it is well known that the cubic form of HfO₂ is dynamically unstable with respect to oxygen shuffles [38]. The lower symmetry polymorphs, in contrast, are stable with respect to small displacements

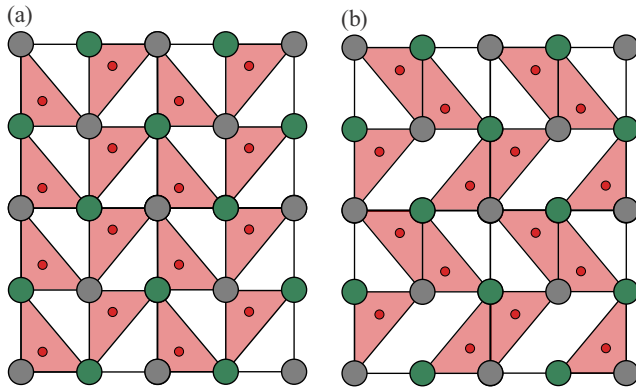


FIG. 6. Projection of the oxygen layer (red atoms) having threefold coordinated Hf atoms in the (a) orthorhombic and (b) monoclinic structures. The green and grey Hf atoms occupy adjacent (200) planes.

and strains and each reside within a local energy well. This is evident in Fig. 7, which collects the results of solid-state nudged elastic band calculations performed between different pairs of HfO₂ polymorphs.

Figure 7 shows that c-HfO₂ has the highest energy of all polymorphs and is a local maximum with respect to a path connecting c-HfO₂ with t-HfO₂. It will, therefore, spontaneously collapse to a tetragonal variant (at zero Kelvin). The tetragonal variant t-HfO₂ resides in a shallow energy well and is separated by a small barrier from m-HfO₂. The monoclinic form, m-HfO₂, has the lowest energy among the four polymorphs considered here. A large barrier separates m-HfO₂ from o-HfO₂, with the latter having an energy between that of t-HfO₂ and m-HfO₂. Figure 7 also shows the energy along a path that connects o-HfO₂ and t-HfO₂. The tetragonal form, t-HfO₂, again resides in a shallow well with respect to this path.

It is instructive to track the strains of the crystal relative to that of c-HfO₂ along the pathways connecting the different polymorphs of HfO₂. Figure 8 shows a projection of the strain order parameters in the e_2 - e_3 subspace. The transfor-

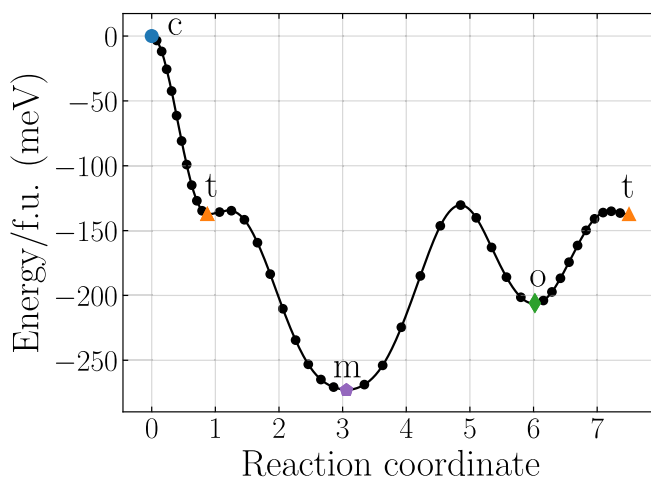


FIG. 7. The energy along pathways connecting different polymorphs of HfO₂. The blue circle corresponds to c-HfO₂, the orange triangles to t-HfO₂, the purple pentagon to m-HfO₂ and the green diamond to o-HfO₂.

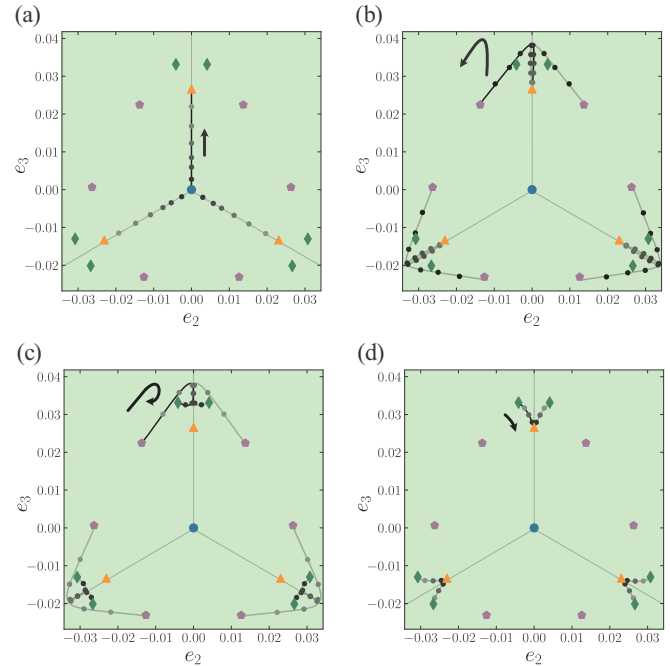


FIG. 8. The strain paths in $e_2 - e_3$ space between (a) c-HfO₂ (at the origin) and the three symmetrically equivalent t-HfO₂ variants (orange triangles), (b) t-HfO₂ and m-HfO₂ (purple pentagons), (c) m-HfO₂ and o-HfO₂ (green diamonds), and (d) o-HfO₂ and t-HfO₂.

mation from c-HfO₂ to t-HfO₂ follows a path corresponding to a simple tetragonal strain as shown in Fig. 8(a). All three symmetrically equivalent paths are shown in Fig. 8(a). Figure 8(b) shows the six symmetrically equivalent minimum energy pathways connecting t-HfO₂ and m-HfO₂ projected in e_2 - e_3 space. The projected strains of the six orientational variants of m-HfO₂ are shown as purple pentagons in Fig. 8. The projections in e_2 - e_3 space represent the tetragonal and orthorhombic strains that must be applied to c-HfO₂ to obtain the monoclinic unit cell. The projection of the strain path between t-HfO₂ and m-HfO₂ follows a curved path. The tetragonal variant is first stretched along its tetragonal axis before picking up an orthorhombic strain. The onset of orthorhombic strains is accompanied by a contraction along the tetragonal axis. A similar path is followed in e_2 - e_3 space when m-HfO₂ transforms to o-HfO₂ as shown in Fig. 8(c). Instead of following the shortest path in e_2 - e_3 space, the crystal first adopts tetragonal symmetry before it becomes orthorhombic. The path connecting t-HfO₂ and o-HfO₂ is shown in Fig. 8(d). Neighboring t-HfO₂ and o-HfO₂ variants are close together in e_2 - e_3 space, and the minimum energy path connecting the polymorphs is almost linear in strain space. In calculating the path between o-HfO₂ and m-HfO₂, care was taken to ensure that the particular oxygen shuffle variant for each polymorph minimized the required atomic displacements to go from o-HfO₂ and m-HfO₂. This was achieved by using a mapping algorithm recently implemented within CASM [74].

C. Pathways between different tetragonal variants

The strain maps in the e_2 - e_3 subspace show that the tetragonal variants, t-HfO₂, serve as hub phases from which clusters

of orientational and translational variants of m-HfO₂ and o-HfO₂ can be obtained. It is, therefore, of interest to explore pathways that connect different orientational variants of t-HfO₂. Figure 9(a) shows the energy along a path connecting a \hat{z} variant of t-HfO₂ to a \hat{y} variant. The pathway connecting different orientational variants of t-HfO₂ of a common c-HfO₂ follows a curved path in e_2 - e_3 space, bypassing the intermediate cubic phase, as shown in Fig. 9(b). The tetragonal shuffle of the oxygen ions also does not pass through the cubic phase, but instead simply rotates from one orientation to another orientation. This can be understood upon inspecting the energy surface of cubic HfO₂ as a function of the phonon modes responsible for the tetragonal oxygen shuffle of t-HfO₂.

Figure 9(c) shows the calculated energy surface of cubic HfO₂ as a function of the oxygen shuffle amplitude and orientation in the space spanned by the \hat{y} and \hat{z} shuffle phonon modes. The origin in Fig. 9(c) corresponds to the cubic phase with oxygen residing at the centers of their tetrahedral interstitial sites (a shuffle amplitude of zero). The energy of the cubic phase is a maximum in this space. The local minima correspond to finite \hat{y} and \hat{z} shuffles. As is clear in Fig. 9(c), these minima are separated by low barriers at finite shuffle amplitude along the dotted-orange lines. While all the shuffle orientations are degenerate in c-HfO₂, a tetragonal distortion along the \hat{z} axis, for example, will favor the $+\hat{z}$ and $-\hat{z}$ shuffles over the $\pm\hat{y}$ and $\pm\hat{x}$ shuffles. Figure 9(c) also makes it clear that a transition from a $+\hat{z}$ -shuffle to a $-\hat{z}$ -shuffle will occur not by passing through a cubic state with a zero shuffle amplitude, but instead through a rotation of the oxygen shuffle through either a $\pm\hat{y}$ or a $\pm\hat{x}$ shuffle. Similar behavior has been predicted for ZrO₂ [78,79].

D. Pathways between different orthorhombic variants

Due to the technological importance of being able to switch the polarization of an orthorhombic variant, we next focus on pathways between different variants of o-HfO₂. We restrict the analysis to pathways between different shuffle variants that all belong to the same orientational variant. There are eight variants for a given orientational variant of the orthorhombic unit cell, leading to seven pathways between unique pairs of translational variants. We explored pathways between the variants of Fig. 4, which are all derived from a \hat{z} t-HfO₂ upon application of an orthorhombic strain with a negative e_2 . Table I summarizes the results. For most pairs, the minimum energy path passes through one or more tetragonal variants. One exception is the path connecting variants 1 and 5 of Fig. 4, which passes through an intermediate orthorhombic phase.

As already noted by Qi *et al.* [49], the complexity of the path between translational variants of o-HfO₂ is sensitive to the particular $\pm\hat{z}$ t-HfO₂ shuffle that the two end-state orthorhombic variants have been derived from. If the end states derive from the same \hat{z} shuffle (i.e., they have the same amplitude of the X_2^- phonon mode of c-HfO₂), then the path connecting the two orthorhombic shuffles passes through a single tetragonal variant with the same \hat{z} shuffle. Figure 10(a) shows the energy for these paths as calculated with the solid-state nudged elastic band method. A shallow

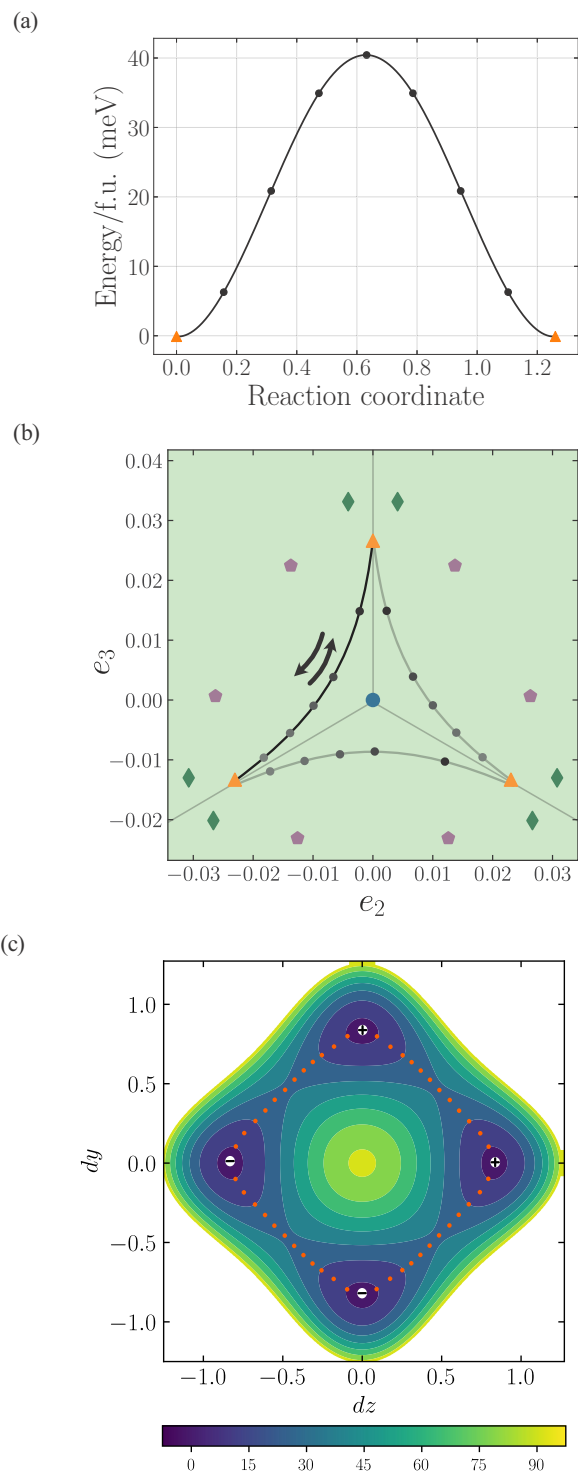


FIG. 9. (a) Energy along the minimum-energy path between two orientational variants of t-HfO₂. (b) Strain in $e_2 - e_3$ space along the minimum energy path connecting $\pm\hat{z}$ and $\pm\hat{y}$ tetragonal variants. The minimum energy path connecting a $+\hat{z}$ variant with a $-\hat{z}$ variant passes through a $\pm\hat{y}$ or $\pm\hat{x}$ variant. (c) Energy landscape of c-HfO₂ as a function of \hat{z} and \hat{y} shuffle order parameters (in meV). The + and - signs indicate translational variants for the same shuffle direction. The orange dots trace the minimum energy path between $\pm\hat{y}/\hat{z}$ and $\mp\hat{y}/\hat{z}$ shuffles.

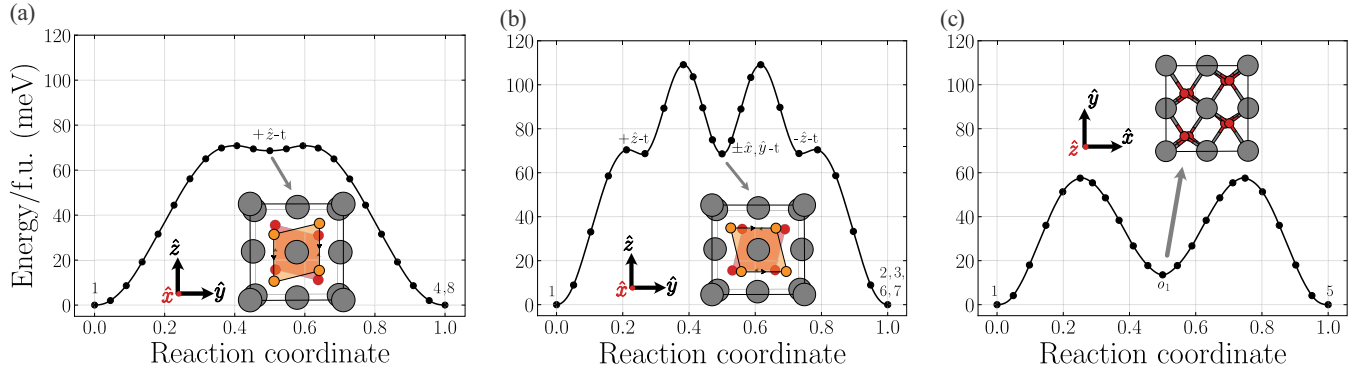


FIG. 10. Minimum energy paths as calculated with the *ss*-NEB method between different shuffle variants of o-HfO₂. Energy along paths connecting o-HfO₂ variants having (a) the same \hat{z} shuffle, (b) different \hat{z} shuffle, and (c) variants 1 and 5, which have the same \hat{z} shuffle, but are found to have the o_1 intermediate state, shown as an inset.

barrier separates the intermediate tetragonal variant from the more stable orthorhombic variants. This pathway is the same as found by Qi *et al.*, Wu *et al.*, and Barabash *et al.* [49,56,59] between translational variants of o-HfO₂ that contain the same t-HfO₂ oxygen shuffle phonon mode. The polarization along this path, for pairs of o-HfO₂ variants that have opposite polarization vectors, varies almost linearly from +45.75 $\mu\text{C}/\text{cm}^2$ to -45.75 $\mu\text{C}/\text{cm}^2$, passing through 0 when the crystal adopts the t-HfO₂ structure at the midpoint of the path, as shown in Fig. S1(d) within the Supplemental Material [80].

When the orthorhombic end states are derived from a different tetragonal shuffle (e.g., one with a $+\hat{z}$ shuffle and the other with a $-\hat{z}$ shuffle), the path first takes the orthorhombic variant to its nearest tetragonal shuffle, which then must transform to the oppositely oriented tetragonal shuffle. As described in the previous section, the minimum energy path between translational variants of the same tetragonal shuffle (e.g., between $+\hat{z}$ and $-\hat{z}$) is through a differently oriented tetragonal shuffle (i.e., a \hat{y} or an \hat{x} shuffle). An example of the energy along such a path as calculate with *ss*-NEB is shown in Fig. 10(b). A similar path was found by Huan *et al.* and Wu *et al.* [38,56], while the path reported by Qi *et al.* and Barabash *et al.* [49,59] does not pass through a differently oriented tetragonal variant, but instead passes through the higher energy cubic state (i.e., c-HfO₂). The polarization along this path when the pair of o-HfO₂ variants have opposite

polarization vectors varies linearly from +45.75 $\mu\text{C}/\text{cm}^2$ to 0 upon adopting the $+\hat{z}$ shuffle of t-HfO₂, then remains zero as the $+\hat{z}$ shuffle transforms to the $-\hat{z}$ shuffle by passing through a \hat{y} shuffle, and again varies linearly from 0 to -45.75 $\mu\text{C}/\text{cm}^2$. This is shown in Fig. S1(e) within the Supplemental Material [80].

There is only one path that did not pass through one or more t-HfO₂ intermediate states. The path connects variants 1 and 5 of Fig. 4. Both shuffle variants, which have an opposite polarization, are derived from the same \hat{z} shuffle, but the path connecting the two variants nevertheless passes through an intermediate polymorph that is locally stable and has a lower energy than the tetragonal polymorph. The energy along the path connecting this pair as calculated with *ss*-NEB is shown in Fig. 10(c). The intermediate state, shown as an inset in Fig. 10(c), has an orthorhombic symmetry and consists of exclusively threefold coordinated oxygen. It is nonpolar and belongs to the Pbcn space group. Here we label the structure o_1 -HfO₂. The lattice parameters a , b , and c as predicted with SCAN are 4.87 Å, 5.17 Å, and 5.70 Å respectively. The coordinates of o_1 -HfO₂ are collected in Table I within the Supplemental Material [80]. Its lattice parameters are very different from those of the other polymorphs as is evident in e_2 - e_3 space, shown in Fig. 11. The polarization along this path varies almost linearly between +45.75 $\mu\text{C}/\text{cm}^2$ and -45.75 $\mu\text{C}/\text{cm}^2$, passing through 0 halfway along the path when the crystal adopts the o_1 -HfO₂ structure, as shown in Fig. S1(f) within the Supplemental Material [80].

The energy along the three distinct paths connecting translational variants of o-HfO₂ in Fig. 10 represent a lower bound. This is because both the lattice vectors and the internal coordinates were allowed to relax during the *ss*-NEB calculations. In reality, epitaxial and/or coherency constraints will limit the degree with which the lattice vectors can relax. As is clear in the strain maps of Figs. 9(b) and 11, the lattice vectors of the crystal vary substantially along the minimum energy pathways between different translational variants. To assess the degree with which the pathways between translation variants of o-HfO₂ may change qualitatively when lattice vectors are not free to relax due to external mechanical constraints, we also calculated the minimum energy paths keeping the unit cell vectors fixed at their values in the o-HfO₂

TABLE I. Various intermediate states along the minimum energy path between variant 1 and the 7 other orthorhombic variants having the same unit cell orientation. t indicates the tetragonal phase whereas o_1 refers to a metastable orthorhombic structure. $\pm\hat{x}$, \hat{y} , or \hat{z} shows the direction of oxygen shuffle in the tetragonal phase.

| Transformation paths | Intermediate states |
|----------------------|--|
| 1 \rightarrow 2 | $+\hat{z} t \rightarrow \pm\hat{x}/\hat{y} t \rightarrow -\hat{z} t$ |
| 1 \rightarrow 3 | $+\hat{z} t \rightarrow \pm\hat{x}/\hat{y} t \rightarrow -\hat{z} t$ |
| 1 \rightarrow 4 | $+\hat{z} t$ |
| 1 \rightarrow 5 | o_1 |
| 1 \rightarrow 6 | $+\hat{z} t \rightarrow \pm\hat{x}/\hat{y} t \rightarrow -\hat{z} t$ |
| 1 \rightarrow 7 | $+\hat{z} t \rightarrow \pm\hat{x}/\hat{y} t \rightarrow -\hat{z} t$ |
| 1 \rightarrow 8 | $+\hat{z} t$ |

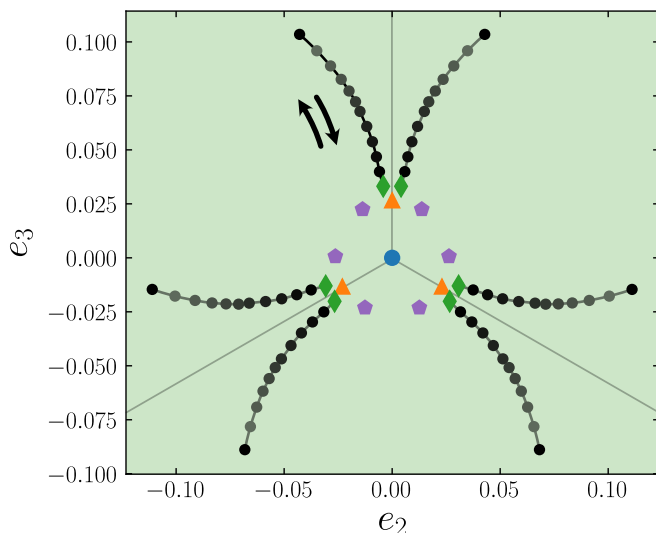


FIG. 11. Strain path in $e_2 - e_3$ space traversed upon going from variant 1 to variant 5. The end point of the path corresponds to the strain of o_1 (relative to c -HfO₂).

crystal structure. The results are summarized in Fig. S1 within the Supplemental Material [80]. The paths that pass through t -HfO₂ in the fully relaxed case were found to also pass through the same t -HfO₂ variants when the lattice vectors were constrained. Nevertheless, the energy along the constrained path is higher than that along the fully relaxed path. The path connecting variants 1 and 5, which passes through the o_1 -HfO₂ structure in the fully relaxed case, does change qualitatively when the lattice vectors are fixed to those of o -HfO₂. Instead of passing through the o_1 -HfO₂, the midpoint adopts a \hat{z} -shuffled t -HfO₂ structure. Even when the midpoint between variants 1 and 5 were initialized in o_1 -HfO₂ the structure spontaneously relaxed to t -HfO₂ when the o -HfO₂ lattice vectors were imposed on each image along the path.

E. Antiphase boundaries

A large grain of HfO₂ can consist of multiple orientational and shuffle variants of o -HfO₂. The interfaces separating one variant from another are usually only several atomic layers thick. Those separating different orientational variants are referred to as twin boundaries, while those separating a pair of shuffle variants of the same orientational variant are referred to as antiphase boundaries (APB). Here we explore the atomic structure within planar antiphase boundaries. The results of the previous section provide guidance in the determination of the atomic structure within an APB.

In studying an APB thermodynamically, we follow a Gibbsian approach that relies on thermodynamic excess quantities [81,82]. The excess energy of an APB, for example, is the energy of a crystal with an APB minus the energy of a crystal without an APB, where both crystals have the same number of atoms and are subjected to identical thermodynamic boundary conditions. Care must be exercised in precisely specifying mechanical boundary conditions.

Since the antiphase boundary is only at most several atomic layers thick, it will adjust its dimensions to match the equilib-

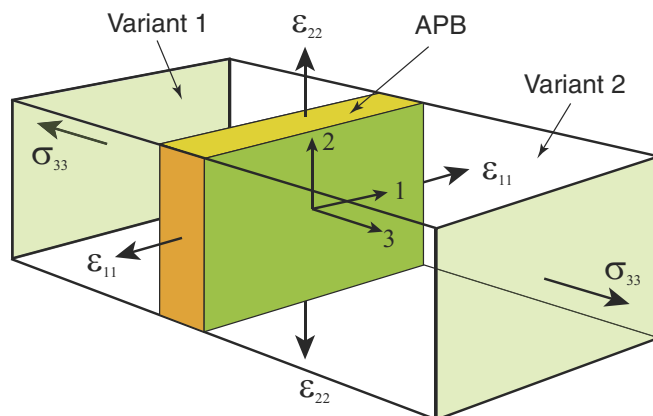


FIG. 12. Mechanical boundary conditions on an antiphase boundary (APB).

rium lattice parameters of the adjacent orthorhombic domains in a plane parallel to the APB. No such epitaxial constraints exist perpendicular to the antiphase boundary plane, however, as the atoms are free to relax until a uniform stress is achieved perpendicular to the APB. The thermodynamic boundary conditions are, therefore, constant strain parallel to the plane of the APB and constant stress perpendicular to the plane of the APB. Using an orthonormal coordinate system in which axes 1 and 2 are in the plane of the APB and axis 3 is perpendicular to the APB, as illustrated in Fig. 12, these boundary conditions correspond to constant strain ϵ_{11} , ϵ_{22} and constant stress σ_{33} . Here we only consider high symmetry orientations of the APB relative to the coexisting polymorph crystal structures such that we can neglect shear strains and stresses. To streamline notation we also set $\sigma_{33} = \sigma$.

The appropriate characteristic potential (i.e., free energy) for the mechanical boundary conditions of an APB is obtained upon application of a Legendre transform to the energy, e , with respect to the normal stress, σ , according to

$$\lambda = e - L\sigma, \quad (2)$$

where L is the length of the crystal perpendicular to the APB. The characteristic potential λ is known as the grand-force potential [81,82]. All three quantities, λ , e , and σ , are normalized by the area of the APB in a fixed reference state (e.g., the equilibrium dimensions of the orthorhombic phase).

The *excess* grand-force potential measures the difference in the free energy between a crystal with an APB and one without an APB and is defined as

$$\Delta\lambda(\sigma) = \lambda^{\text{APB}}(\sigma) - \lambda(\sigma) \quad (3)$$

where λ^{APB} and λ are the free energies of the crystal with and without an APB, respectively. All potentials in the above equation are also functions of the strains parallel to the APB (i.e., ϵ_{11} and ϵ_{22}), but the explicit dependence on strain is dropped to simplify notation. The excess grand-force potential $\Delta\lambda$ constitutes the free energy cost of an APB as a function of the stress σ normal to the APB and the strains ϵ_{11} and ϵ_{22} , parallel to the APB.

Other thermodynamic excess quantities associated with an APB can be considered. For example, an APB may swell or

contract perpendicular to the APB plane relative to a perfect crystal without an APB. This is measured with the APB excess thickness, defined as

$$\Delta L(\sigma) = L^{\text{APB}}(\sigma) - L(\sigma) \quad (4)$$

where L^{APB} and L are the lengths of the crystal perpendicular to the APB of a crystal with and without an APB, respectively. It can be shown that the excess thickness of the APB is related to the excess grand-force potential according to

$$\frac{\partial \Delta \lambda}{\partial \sigma} = -\Delta L. \quad (5)$$

If ΔL is greater (less) than zero, then tensile stresses will decrease (increase) the excess free energy of the APB.

The excess free energy of an APB can be obtained by calculating the energy of large super cells with and without APBs. Because of periodic boundary conditions, a super cell containing two different variants of o-HfO₂ will necessarily have two APBs. The super cell should be long in a direction perpendicular to the APB to maximize the distance between APBs and their periodic images. To minimize k -point errors of the DFT calculations, a similar super cell is used to calculate the energy of o-HfO₂ without APBs. Depending on the orientation of the APB, we used a super cell consisting of either $1 \times 1 \times 8$ or $9 \times 1 \times 1$ unit cells of o-HfO₂.

The first step to obtain the excess grand-force potential $\Delta \lambda$ is to calculate the energy E of the super cell as a function of L , the super cell length perpendicular to the APB, while allowing for internal atomic relaxations. This is shown in Fig. 13(a) for an APB separating variants 1 and 5 of Fig. 4. Variants 1 and 5 derive from the same translational shuffle of t-HfO₂ but have oppositely oriented polarizations. According to Qi *et al.* [49], this makes it possible to move the boundary separating the two variants with an electric field. As shown in the previous section, a homogeneous transformation of variant 1 into variant 5 passes through the o₁ structure. Since the o₁ structure has a strain state that differs substantially from that of o-HfO₂, its stability within the APB will be very sensitive to the local strain state.

The energy in Fig. 13(a) is for a planar APB that is perpendicular to the \hat{z} axis (i.e., the c lattice vector of the orthorhombic unit cell). The APB is therefore perpendicular to the tetragonal axis and shuffle direction of the tetragonal variant from which the o-HfO₂ variants 1 and 5 are derived. The blue curve in Fig. 13(a) is the energy of a $1 \times 1 \times 8$ super cell of o-HfO₂ without an APB as a function of the long length L . The green curve is the energy of the same super cell containing two symmetrically equivalent APBs separating variants 1 and 5. The slope of the energy as a function of L in Fig. 13(a), when normalized by the area of the APB, is equal to the stress σ , which can then be used to calculate the grand-force potential λ according to Eq. (2). The green curve in Fig. 13(b) corresponds to the resulting excess grand-force potential, Eq. (3), as a function of stress σ . At $\sigma = 0$, the cost to create an APB is $\Delta \lambda = 0.378 \text{ J/m}^2$, a high value for a coherent interface. The grand-force potential has a negative slope, signifying a positive excess length. At zero stress, the excess length $\Delta L = 0.238 \text{ \AA}$. Figure 14(a) shows the relaxed structure within the APB separating variants 1 and 5. The atoms within the APB were initialized as having either a local

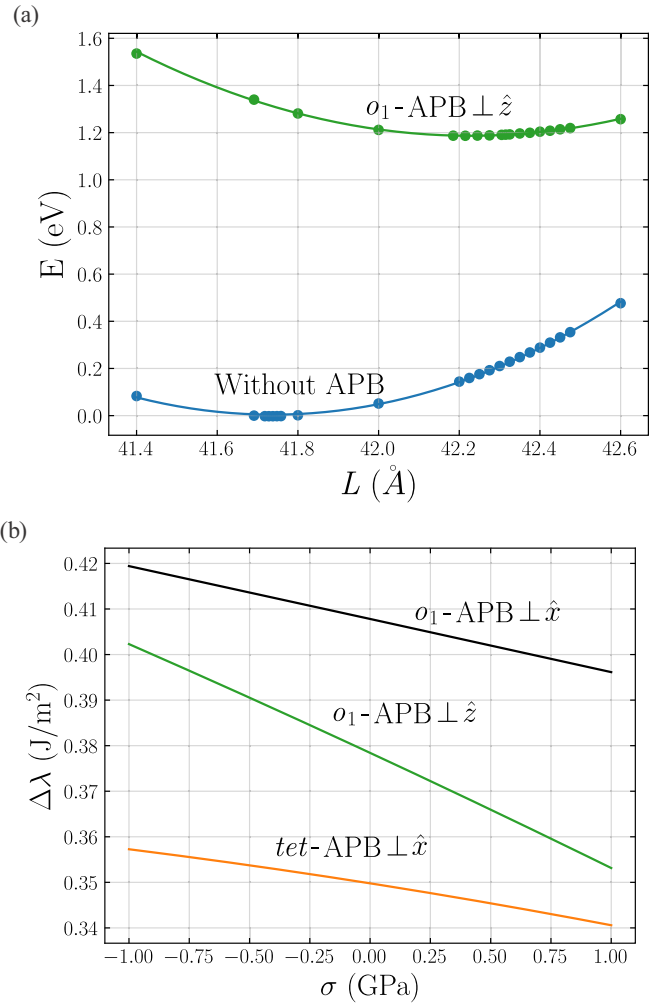


FIG. 13. (a) Energy of $1 \times 1 \times 8$ super cells of the unit cell of a o-HfO₂ variant derived from a \hat{z} tetragonal variant. The long direction is parallel to the \hat{z} direction. The blue curve is for a super cell without an APB while the green curve is for a super cell containing two translational variants of o-HfO₂ separated by two APBs. (b) The free energy (grand-force potential) of different APBs as a function of stress perpendicular to the APB.

tetragonal structure or an o₁ structure. Both initializations, however, relaxed to the same APB having a local o₁ structure, being approximately one unit cell thick.

It is instructive to also consider a different orientation of the flat APB separating the same variants 1 and 5. We considered an APB that is perpendicular to the \hat{x} direction for variants 1 and 5 of Fig. 4 (i.e., perpendicular to the a lattice vector of the orthorhombic unit cell). For this orientation, we used a $9 \times 1 \times 1$ super cell to ensure that the two APBs within the super cell are symmetrically equivalent to each other. As before, the structure within the APB was initialized to that of o₁ in one set of calculations and to that of t-HfO₂ having a \hat{z} shuffle in another set of calculations. In contrast to the APB that is perpendicular to the \hat{z} direction (i.e., c lattice vector of the orthorhombic cell), the local structure of the APB perpendicular to the \hat{x} direction (i.e., the a lattice vector of the orthorhombic cell) was found to remain (meta) stable in both

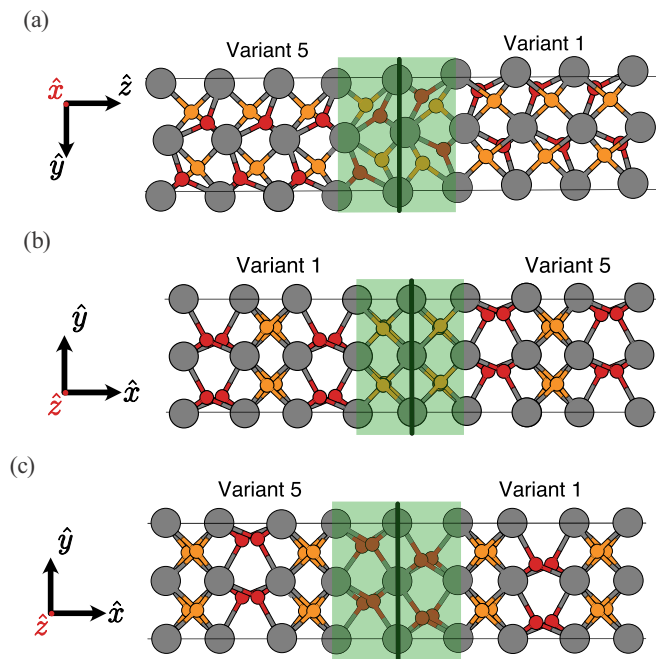


FIG. 14. Relaxed structures of APBs between variants 1 and 5 derived from a \hat{z} tetragonal variant. (a) An APB perpendicular to the \hat{z} direction with a local o_1 atomic structure; (b) an APB perpendicular to the \hat{x} direction with a local tetragonal structure (shuffled along the \hat{z} direction); and (c) an APB perpendicular to the \hat{x} direction with an o_1 structure.

the t-HfO₂ and the o_1 -HfO₂ structures. The relaxed structures of the two APB models are shown in Figs. 14(b) and 14(c).

The calculated excess grand-force potentials $\Delta\lambda$ as a function of σ for the two APB structures are shown in Fig. 13(b) and are compared to the excess grand-force potential of the APB perpendicular to the \hat{z} direction. As is clear from Fig. 13(b), the APB with the lowest $\Delta\lambda(\sigma)$ has an atomic shuffle that is similar to that of t-HfO₂. When perpendicular to the \hat{x} direction, the APB with a local t-HfO₂ structure has an excess free energy that is significantly lower than that of the APB with a local o_1 structure. Furthermore, the APB that is perpendicular to the \hat{x} direction with a local t-HfO₂ structure is more stable than the APB that is perpendicular to the \hat{z} direction, which has a local o_1 structure.

The switch in the lowest energy local structure within the APB upon a change in the orientation of the APB can be attributed to a change in the epitaxial strain state imposed by the adjacent orthorhombic variants on the APB. The epitaxial constraints imposed upon the thin region that constitutes the APB by the surrounding o-HfO₂ domains is very different for the two APB orientations. Since the t-HfO₂ and the o_1 -HfO₂ structures adopt very different equilibrium strains relative to o-HfO₂, their stability will be sensitive to the externally imposed strain constraints, which varies with the orientation of the APB.

IV. DISCUSSION

Hafnia, and in particular its recently discovered ferroelectric polymorph, is of tremendous interest for microelectronic

applications [28,29]. Thin films of HfO₂ often consist of mixtures of symmetrically equivalent variants of different polymorphs that coexist coherently within the same grain [42]. This can occur since important polymorphs such as t-HfO₂, m-HfO₂, and o-HfO₂ are all derived from a common high-symmetry c-HfO₂ crystal through small symmetry breaking structural distortions.

In this paper we have clarified the relationship between the different polymorphs of HfO₂ and their symmetrically equivalent variants with the help of symmetry-adapted strain-order parameters [75,83]. The subspace spanned by the e_2 and e_3 strain-order parameters (Fig. 1), which describes tetragonal and orthorhombic distortions of the cubic reference crystal, is especially informative in that it clearly displays the relationship between different orientational variants of each polymorph. The e_2 - e_3 subspace reveals the key role played by the three orientational variants of t-HfO₂, with each tetragonal variant serving as a hub from which multiple variants of the lower symmetry m-HfO₂ and o-HfO₂ polymorphs can be derived. Strain order-parameter maps, such as Fig. 1, which chart the strains of symmetrically equivalent variants of different polymorphs relative to c-HfO₂, also give an indication of the degree with which different variants must be distorted to achieve coherent coexistence within the same grain.

Ferroelectric switching of o-HfO₂ in an applied electric field is realized by the growth of domains with favorably oriented polarizations at the expense of domains with less favorably aligned polarizations [44–48]. This is achieved through the migration of the boundaries separating different variants that coexist within the same grain. A distinction can be made between twin boundaries, which separate different orientational variants of o-HfO₂, and antiphase boundaries, which separate different translational variants that nevertheless have the same orientation of their unit cell. The local atomic structure within a boundary plays an important role in determining the energy cost of forming the boundary as well as the mobility of the boundary.

The results of this paper show that the atomic structure of an APB is often very similar to the intermediate structure along pathways that homogeneously convert one variant into another. In addition to confirming several pathways discovered in previous papers [38,49–59], we have also found new pathways having a lower energy. The tetragonal phase t-HfO₂ plays an important role in many of the pathways connecting different translational variants of o-HfO₂. However, for one pair of o-HfO₂ variants we discovered a different intermediate phase that is locally stable and has orthorhombic symmetry.

The actual structure and energy cost of an APB can be calculated with a super cell consisting of two variants separated by a pair of APBs. This approach has been applied in multiple studies to investigate domain boundary structures and energies between different variants of o-HfO₂ [49–51]. In this paper we have used a method to analyze the thermodynamic properties of a domain boundary that relies on Gibbsian excess quantities [81]. When calculating excess quantities, such as the free energy of an APB, it is crucial that identical thermodynamic boundary conditions are imposed in the crystals with and without the APB. A common practice is to calculate the energy difference between a super cell with an APB and one without an APB at constant L , the length of the super cell

perpendicular to the APB. However, this difference in energy is generally not a meaningful quantity since neither the stress state nor the strain state within the orthorhombic variants in the regions adjacent to the APB are the same as that of the homogeneous reference state. If energies with and without the APB are not calculated at the same stress perpendicular to the APB, a spurious elastic energy within the adjacent domains is included in the excess free energy of the APB that is not related to the cost of creating the APB.

Our calculations show that the energy and atomic structure of an APB can be very sensitive to the orientation of the APB, even when the APB separates the same two variants. This is in large part due to the different epitaxial strain constraints imposed on the thin APB layer by the adjacent orthorhombic domains when reorienting the plane of the APB. As revealed by our calculations, variations in the epitaxial strain constraints can lead to a qualitative change in the atomic structure within the APB, which in turn determines the energy of the APB. Highly anisotropic APB energies will play a role in determining the types of microstructures that appear in grains of multiple translational variants of ferroelectric HfO₂. We expect that a change in the local atomic structure of an APB as it reorients will also lead to a strong orientation dependence of the APB mobility. This will be topic for a future study.

The thermodynamic properties calculated in this paper are strictly only valid at zero Kelvin. While we expect that the qualitative trends predicted here remain valid at room temperature, the sequence of phase transitions with temperature between different polymorphs of HfO₂ clearly indicate that entropic contributions to the free energies of each polymorph are of significant importance, especially at elevated temperature. The primary source of entropy in HfO₂ can be attributed to vibrational excitations. The high temperature stability of the cubic phase, c-HfO₂, for example, must arise from large-scale anharmonic vibrational excitations as this polymorph is predicted to be dynamically unstable at zero Kelvin. Similar to other high temperature phases that become dynamically unstable at low temperatures, a statistical mechanics treatment of vibrational excitations must go beyond the (quasi-) harmonic approximation and explicitly account for anharmonicity to adequately describe the high temperature thermodynamic properties of c-HfO₂ [84–90]. Vibrational excitations also play a crucial role in stabilizing the tetragonal phase, t-HfO₂, at intermediate temperatures as a sizable entropic contribution is necessary to overcome the large difference in energy between t-HfO₂ and the low temperature m-HfO₂ polymorph. The strong temperature dependence of the free energies of each polymorph will have implications for the structural pathways and free energy barriers between

polymorphs and for the thermodynamic properties and atomic structures of APBs at elevated temperature. Due to the high temperature stability of t-HfO₂, an increase in temperature will decrease the free energy of t-HfO₂ more so than the free energies of o-HfO₂ and m-HfO₂. The excess free energies of APBs having a local t-HfO₂ structure are therefore also likely to decrease with increasing temperature. Furthermore, APBs separating translational variants of o-HfO₂ having a local t-HfO₂ structure may serve as heterogeneous nucleation sites for the transformation to t-HfO₂ at elevated temperature. The temperature dependent properties of APBs having the o₁-HfO₂ structure are at this point not clear and will require an analysis of the vibrational properties of the o₁-HfO₂ polymorph relative to those of t-HfO₂ and o-HfO₂.

V. CONCLUSIONS

We have shown how symmetry-adapted strain-order parameters can clarify the relationship between different HfO₂ polymorphs and their multiple translational and orientational variants. First-principles calculations were performed to map out minimum energy pathways between different polymorphs and their variants in subspaces of the symmetry adapted strain order parameters. The intermediate states along paths that homogeneously convert one translational variant of ferroelectric HfO₂ into another can guide the search for the atomic structure within the domain boundaries separating different variants. In studying the thermodynamic properties and equilibrium structure of antiphase boundaries, we used an approach that relies on Gibbsian excess quantities. Our first-principles analysis of domain boundaries separating translational variants of ferroelectric HfO₂ has shown that the domain boundary energy can be highly anisotropic due to changes in the epitaxial strain constraints with the orientation of the boundary.

ACKNOWLEDGMENTS

This work was supported by the NSF IDEAS center, Grant No. 1934641. Use was made of computational facilities purchased with funds from the National Science Foundation (CNS-1725797) and administered by the Center for Scientific Computing (CSC). The CSC is supported by the California NanoSystems Institute and the Materials Research Science and Engineering Center (MRSEC; NSF DMR 1720256) at UC Santa Barbara. We are also grateful for computing resources from the National Energy Research Scientific Computing Center (NERSC), a U.S. Department of Energy Office of Science User Facility operated under Contract No. DE-AC02-05CH11231 using NERSC award BES-ERCAP0020609.

-
- [1] N. Setter, D. Damjanovic, L. Eng, G. Fox, S. Gevorgian, S. Hong, A. Kingon, H. Kohlstedt, N. Park, G. Stephenson *et al.*, *J. Appl. Phys.* **100**, 051606 (2006).
 - [2] S.-Y. Wu, *IEEE Trans. Electron Devices* **21**, 499 (1974).
 - [3] J. Hoffman, X. Pan, J. W. Reiner, F. J. Walker, J. P. Han, C. H. Ahn, and T. P. Ma, *Adv. Mater.* **22**, 2957 (2010).
 - [4] D. H. Looney, US Patent No. 2,791,758 (1957).
 - [5] H. Koike, US Patent No. 5,600,587 (1997).
 - [6] T. Mikolajick, S. Slesazek, M. H. Park, and U. Schroeder, *MRS Bull.* **43**, 340 (2018).
 - [7] J. Junquera and P. Ghosez, *Nature (London)* **422**, 506 (2003).
 - [8] M. Dawber, K. M. Rabe, and J. F. Scott, *Rev. Mod. Phys.* **77**, 1083 (2005).

- [9] D. A. Muller, T. Sorsch, S. Moccio, F. Baumann, K. Evans-Lutterodt, and G. Timp, *Nature (London)* **399**, 758 (1999).
- [10] D. D. Fong, G. B. Stephenson, S. K. Streiffer, J. A. Eastman, O. Auciello, P. H. Fuoss, and C. Thompson, *Science* **304**, 1650 (2004).
- [11] D. Tenne, A. Bruchhausen, N. Lanzillotti-Kimura, A. Fainstein, R. Katiyar, A. Cantarero, A. Soukiassian, V. Vaithyanathan, J. Haeni, W. Tian *et al.*, *Science* **313**, 1614 (2006).
- [12] D. G. Schlom, S. Guha, and S. Datta, *MRS Bull.* **33**, 1017 (2008).
- [13] H. Liu and X. Yang, *Ferroelectrics* **507**, 69 (2017).
- [14] C. Ahn, K. Rabe, and J.-M. Triscone, *Science* **303**, 488 (2004).
- [15] N. Nuraje and K. Su, *Nanoscale* **5**, 8752 (2013).
- [16] A. von Hippel, R. Breckenridge, F. Chesley, and L. Tisza, *Ind. Eng. Chem.* **38**, 1097 (1946).
- [17] L. Davis Jr. and L. G. Rubin, *J. Appl. Phys.* **24**, 1194 (1953).
- [18] T. Mitsui and W. B. Westphal, *Phys. Rev.* **124**, 1354 (1961).
- [19] Ph. Ghosez, E. Cockayne, U. V. Waghmare, and K. M. Rabe, *Phys. Rev. B* **60**, 836 (1999).
- [20] J. W. Reiner, A. M. Kolpak, Y. Segal, K. F. Garrity, S. Ismail-Beigi, C. H. Ahn, and F. J. Walker, *Adv. Mater.* **22**, 2919 (2010).
- [21] M. D. McDaniel, T. Q. Ngo, S. Hu, A. Posadas, A. A. Demkov, and J. G. Ekerdt, *Appl. Phys. Rev.* **2**, 041301 (2015).
- [22] M. Okuyama and Y. Hamakawa, *Ferroelectrics* **63**, 243 (1985).
- [23] R. E. Cohen and H. Krakauer, *Ferroelectrics* **136**, 65 (1992).
- [24] V. Bhide, K. Deshmukh, and M. Hegde, *Physica* **28**, 871 (1962).
- [25] H. H. Sønsteby, H. Fjellvåg, and O. Nilsen, *Adv. Mater. Interfaces* **4**, 1600903 (2017).
- [26] T. Böske, J. Müller, D. Bräuhaus, U. Schröder, and U. Böttger, *Appl. Phys. Lett.* **99**, 102903 (2011).
- [27] T. Böske, S. Teichert, D. Bräuhaus, J. Müller, U. Schröder, U. Böttger, and T. Mikolajick, *Appl. Phys. Lett.* **99**, 112904 (2011).
- [28] S. J. Kim, J. Mohan, S. R. Summerfelt, and J. Kim, *JOM* **71**, 246 (2019).
- [29] M. H. Park, Y. H. Lee, T. Mikolajick, U. Schroeder, and C. S. Hwang, *Adv. Electron. Mater.* **5**, 1800522 (2019).
- [30] X. Sang, E. D. Grimley, T. Schenk, U. Schroeder, and J. M. LeBeau, *Appl. Phys. Lett.* **106**, 162905 (2015).
- [31] X. Tian, S. Shibayama, T. Nishimura, T. Yajima, S. Migita, and A. Toriumi, *Appl. Phys. Lett.* **112**, 102902 (2018).
- [32] S. S. Cheema, D. Kwon, N. Shanker, R. Dos Reis, S.-L. Hsu, J. Xiao, H. Zhang, R. Wagner, A. Datar, M. R. McCarter *et al.*, *Nature (London)* **580**, 478 (2020).
- [33] H.-J. Lee, M. Lee, K. Lee, J. Jo, H. Yang, Y. Kim, S. C. Chae, U. V. Waghmare, and J. H. Lee, *Science* **369**, 1343 (2020).
- [34] H. J. Kim, M. H. Park, Y. J. Kim, Y. H. Lee, W. Jeon, T. Gwon, T. Moon, K. D. Kim, and C. S. Hwang, *Appl. Phys. Lett.* **105**, 192903 (2014).
- [35] M. H. Park, H. J. Kim, G. Lee, J. Park, Y. H. Lee, Y. J. Kim, T. Moon, K. D. Kim, S. D. Hyun, H. W. Park *et al.*, *Appl. Phys. Rev.* **6**, 041403 (2019).
- [36] K. Lee, H.-J. Lee, T. Y. Lee, H. H. Lim, M. S. Song, H. K. Yoo, D. I. Suh, J. G. Lee, Z. Zhu, A. Yoon *et al.*, *ACS Appl. Mater. Interfaces* **11**, 38929 (2019).
- [37] M. Hoffmann, M. Pešić, K. Chatterjee, A. I. Khan, S. Salahuddin, S. Slesazeck, U. Schroeder, and T. Mikolajick, *Adv. Funct. Mater.* **26**, 8643 (2016).
- [38] T. D. Huan, V. Sharma, G. A. Rossetti Jr, and R. Ramprasad, *Phys. Rev. B* **90**, 064111 (2014).
- [39] L. Azevedo Antunes, R. Ganser, R. Alcalá, T. Mikolajick, U. Schroeder, and A. Kersch, *Appl. Phys. Lett.* **119**, 082903 (2021).
- [40] A. Raeliarijaona and R. Cohen, [arXiv:2108.09884](https://arxiv.org/abs/2108.09884).
- [41] R. Materlik, C. Künneth, and A. Kersch, *J. Appl. Phys.* **117**, 134109 (2015).
- [42] E. D. Grimley, T. Schenk, T. Mikolajick, U. Schroeder, and J. M. LeBeau, *Adv. Mater. Interfaces* **5**, 1701258 (2018).
- [43] M. Pešić, F. P. G. Fengler, L. Larcher, A. Padovani, T. Schenk, E. D. Grimley, X. Sang, J. M. LeBeau, S. Slesazeck, U. Schroeder *et al.*, *Adv. Funct. Mater.* **26**, 4601 (2016).
- [44] Y.-H. Shin, I. Grinberg, I.-W. Chen, and A. M. Rappe, *Nature (London)* **449**, 881 (2007).
- [45] H. Stadler and P. Zachmanidis, *J. Appl. Phys.* **34**, 3255 (1963).
- [46] W. J. Merz, *Phys. Rev.* **95**, 690 (1954).
- [47] S. Liu, I. Grinberg, and A. M. Rappe, *Nature (London)* **534**, 360 (2016).
- [48] T. Tybell, P. Paruch, T. Giamarchi, and J.-M. Triscone, *Phys. Rev. Lett.* **89**, 097601 (2002).
- [49] Y. Qi, S. Singh, and K. M. Rabe, [arXiv:2108.12538](https://arxiv.org/abs/2108.12538).
- [50] D.-H. Choe, S. Kim, T. Moon, S. Jo, H. Bae, S.-G. Nam, Y. S. Lee, and J. Heo, *Mater. Today* **50**, 8 (2021).
- [51] W. Ding, Y. Zhang, L. Tao, Q. Yang, and Y. Zhou, *Acta Mater.* **196**, 556 (2020).
- [52] R. Batra, H. D. Tran, and R. Ramprasad, *Appl. Phys. Lett.* **108**, 172902 (2016).
- [53] R. Batra Jr., T. D. Huan, J. L. Jones, G. Rossetti Jr, and R. Ramprasad, *J. Phys. Chem. C* **121**, 4139 (2017).
- [54] Y. Qi and K. M. Rabe, *Phys. Rev. B* **102**, 214108 (2020).
- [55] X. Xu, F.-T. Huang, Y. Qi, S. Singh, K. M. Rabe, D. Obeysekera, J. Yang, M.-W. Chu, and S.-W. Cheong, *Nat. Mater.* **20**, 826 (2021).
- [56] J. Wu, *J. Phys.: Condens. Matter* **33**, 295501 (2021).
- [57] S. Clima, D. Wouters, C. Adelman, T. Schenk, U. Schroeder, M. Jurczak, and G. Pourtois, *Appl. Phys. Lett.* **104**, 092906 (2014).
- [58] K. Z. Rushchanskii, S. Blügel, and M. Ležaić, *Phys. Rev. Lett.* **127**, 087602 (2021).
- [59] S. V. Barabash, D. Pramanik, Y. Zhai, B. Magyari-Kope, and Y. Nishi, *ECS Transactions* **75**, 107 (2017).
- [60] G. Kresse and J. Hafner, *Phys. Rev. B* **47**, 558 (1993).
- [61] G. Kresse and J. Furthmüller, *Comput. Mater. Sci.* **6**, 15 (1996).
- [62] G. Kresse and J. Furthmüller, *Phys. Rev. B* **54**, 11169 (1996).
- [63] P. E. Blöchl, *Phys. Rev. B* **50**, 17953 (1994).
- [64] G. Kresse and D. Joubert, *Phys. Rev. B* **59**, 1758 (1999).
- [65] J. Sun, A. Ruzsinszky, and J. P. Perdew, *Phys. Rev. Lett.* **115**, 036402 (2015).
- [66] J. Sun, R. C. Remsing, Y. Zhang, Z. Sun, A. Ruzsinszky, H. Peng, Z. Yang, A. Paul, U. Waghmare, X. Wu *et al.*, *Nat. Chem.* **8**, 831 (2016).
- [67] R. D. King-Smith and David Vanderbilt, *Phys. Rev. B* **47**, 1651 (1993).
- [68] N. A. Spaldin, *J. Solid State Chem.* **195**, 2 (2012).
- [69] D. Sheppard, P. Xiao, W. Chemelewski, D. D. Johnson, and G. Henkelman, *J. Chem. Phys.* **136**, 074103 (2012).
- [70] D. Sheppard and G. Henkelman, *J. Comput. Chem.* **32**, 1769 (2011).
- [71] G. Henkelman and H. Jónsson, *J. Chem. Phys.* **113**, 9978 (2000).

- [72] G. Henkelman, B. P. Uberuaga, and H. Jónsson, *J. Chem. Phys.* **113**, 9901 (2000).
- [73] D. Sheppard, R. Terrell, and G. Henkelman, *J. Chem. Phys.* **128**, 134106 (2008).
- [74] J. C. Thomas, A. R. Natarajan, and A. Van der Ven, *npj Comput. Mater.* **7**, 164 (2021).
- [75] J. C. Thomas and A. Van der Ven, *J. Mech. Phys. Solids* **107**, 76 (2017).
- [76] J. C. Thomas and A. Van der Ven, *Phys. Rev. B* **96**, 134121 (2017).
- [77] T. Shimizu, K. Katayama, T. Kiguchi, A. Akama, T. J. Konno, O. Sakata, and H. Funakubo, *Sci. Rep.* **6**, 32931 (2016).
- [78] C. Carbogno, C. G. Levi, C. G. Van de Walle, and M. Scheffler, *Phys. Rev. B* **90**, 144109 (2014).
- [79] M.-H. Chen, J. C. Thomas, A. R. Natarajan, and A. Van der Ven, *Phys. Rev. B* **94**, 054108 (2016).
- [80] See Supplemental Material at <http://link.aps.org/supplemental/10.1103/PhysRevMaterials.6.054403> for more information about NEB paths.
- [81] A. Van der Ven and G. Ceder, *Acta Mater.* **52**, 1223 (2004).
- [82] R. A. Enrique and A. Van der Ven, *J. Mech. Phys. Solids* **107**, 494 (2017).
- [83] J. S. Bechtel and A. Van der Ven, *Phys. Rev. Materials* **2**, 025401 (2018).
- [84] J. C. Thomas and A. Van der Ven, *Phys. Rev. B* **88**, 214111 (2013).
- [85] J. C. Thomas and A. Van der Ven, *Phys. Rev. B* **90**, 224105 (2014).
- [86] A. Page, C. Uher, P. F. Poudeu, and A. Van der Ven, *Phys. Rev. B* **92**, 174102 (2015).
- [87] A. Van der Ven, J. C. Thomas, B. Puchala, and A. R. Natarajan, *Annu. Rev. Mater. Res.* **48**, 27 (2018).
- [88] J. C. Thomas, J. S. Bechtel, A. R. Natarajan, and A. Van der Ven, *Phys. Rev. B* **100**, 134101 (2019).
- [89] J. S. Bechtel, J. C. Thomas, and A. Van der Ven, *Phys. Rev. Materials* **3**, 113605 (2019).
- [90] C. Verdi, F. Karsai, P. Liu, R. Jinnouchi, and G. Kresse, *npj Comput. Mater.* **7**, 156 (2021).